

Computational Investigation of Supersonic Boundary Layer Transition over Canonical Fuselage Nose Configurations

M. Choudhari*, N. Tokugawa**, F. Li*, C.-L. Chang*, J. A. White*,
H. Ishikawa†, Y. Ueda‡, T. Atobe**, and K. Fujii**

Corresponding author: Meelan.M.Choudhari@nasa.gov

* NASA Langley Research Center, Hampton, VA, USA

** Japan Aerospace Exploration Agency, Tokyo, JAPAN

† Sanko-Soft Co. Ltd., Tokyo, JAPAN

‡ Tokyo Business Service Co. Ltd., Tokyo, JAPAN.

Abstract: Boundary layer transition over axisymmetric bodies at non-zero angle of attack in supersonic flow is numerically investigated as part of joint research between the National Aeronautics and Space Administration (NASA) and Japan Aerospace Exploration Agency (JAXA). Transition over four axisymmetric bodies (namely, Sears-Haack body, semi-Sears-Haack body, 5-degree straight cone and flared cone) with different axial pressure gradients has been studied at Mach 2 in order to understand the effect of axial pressure gradient on instability amplification along the leeward symmetry plane and in the region of nonzero crossflow away from it. Comparisons are made with measured transition data in Mach 2 facilities as well as with predicted and measured transition characteristics for a 5-degree straight cone in a Mach 3.5 low disturbance tunnel. Limitations of using linear stability correlations for predicting transition over axisymmetric bodies at angle of attack are pointed out.

Keywords: Laminar-turbulent transition, supersonic flows, natural laminar flow.

Nomenclature

(All dimensional quantities in SI units unless specified otherwise.)

A	=	amplitude of instability wave (peak streamwise velocity fluctuation scaled by freestream speed)
C	=	heat capacitance of polysulphone
C_p	=	surface pressure coefficient $(p-p_\infty) / (\frac{1}{2} \rho_\infty U_\infty^2)$
f	=	disturbance frequency
L	=	model length
M	=	Mach number
N	=	logarithmic amplification ratio of instability waves relative to the station where they first begin to amplify (also referred to as N-factor)
n	=	azimuthal wavenumber
P	=	pressure
p'_{RMS}	=	root-mean-square static pressure fluctuation scaled by $\frac{1}{2} \rho_\infty U_\infty^2$
q_w	=	heat flux across model wall
$R(x)$	=	local radius at axial location x
R_{unit}	=	unit Reynolds number
R_x	=	local Reynolds number based on axial coordinate, free-stream velocity, and kinematic viscosity

t	= time
T	= temperature
U	= velocity
x	= axial location with respect to cone apex
(y, z)	= crossplane Cartesian coordinates, such that $z=0$ consists of windward and leeward half planes
α	= angle of attack
δ	= boundary layer thickness
η	= surface-normal coordinate
κ	= thermal conductivity
φ	= circumferential (i.e., azimuthal) angle with respect to the leeward plane of symmetry
ρ	= density
ψ	= the angle of wave number vector of the most amplified disturbance mode with respect to inviscid streamline at the body surface
θ_c	= cone half angle

Abbreviations

AoA	= angle of attack
FC	= flared cone
NLF	= natural laminar flow
QP	= quasi-parallel
QPNC	= quasi-parallel with no effects of streamwise curvature
R.M.S.	= root mean square
SC	= straight cone
SH	= Sears-Haack body
SLDT	= Supersonic Low Disturbance Tunnel
SSH	= semi Sears-Haack body

Subscripts

0	= stagnation condition
∞	= free-stream condition

1 Introduction

Aerodynamic drag reduction is a crucial issue for the economic and environmental viability of the next generation of supersonic aircraft. Laminar flow technology, in particular, offers the greatest potential for improved aerodynamic efficiency, provided that the relevant concept(s) can be integrated into the airframe design without unacceptable penalties in terms of overall vehicle drag or the targeted sonic boom signature.

Over the years, both passive and active forms of laminar flow control have been extensively investigated for aircraft wings, empennage, and nacelles, particularly in the subsonic speed regime.¹ Passive approaches (also known as natural laminar flow and abbreviated as NLF) include the tailoring of surface pressure gradient to reduce the growth rates of boundary layer instability waves, as well as the control of transition by artificially exciting suitable modes of stationary crossflow vortex instability using discrete roughness elements near the lower branch neutral location.² Active techniques utilize surface suction via suction pumps and/or active surface temperature modification to achieve substantial stabilization of the boundary layer flow, albeit at the cost of additional energy input and other penalties related to weight, increased system complexity, and maintenance. Hybrid approaches that combine suction near the wing leading edge with airfoil shaping farther downstream have been shown to provide robust laminar flow control on both subsonic³⁻⁵ and supersonic⁶ aircraft. Despite successful demonstrations, however, neither the purely active nor the hybrid laminar flow control (HLFC) techniques for transition delay over wings have been adopted in practical applications involving commercial or military aircraft.

With rising fuel costs and increased emphasis on the environmental impact of civil aviation, there has been increased attention to incorporating passive laminar flow techniques on new aircraft. Examples include: NLF nacelle and passive HLFC on the stabilizer/fin of Boeing 787⁷ and an NLF wing on the Honda Jet⁸ that maintained a favorable pressure gradient up to 40% chord on the upper surface and 60% on the lower surface. The Honda Jet also included a bulged fuselage nose for NLF

that extended nearly up to the entry door along the lower fuselage. A subscale model of a supersonic transport with modest regions of natural laminar flow over the wings was flight tested during the Supersonic Experimental Airplane (NEXST-1) project by the Japan Aerospace Exploration Agency (JAXA).⁹

For subsonic transports with a fully turbulent flow over most of the surfaces, the overall fuselage drag (including both pressure drag and viscous drag components) accounts for nearly one half of the overall drag.¹⁰ In the presence of substantial laminar flow over the lifting surfaces, the contribution due to fuselage drag rises to approximately 70%.¹⁰ For supersonic aircraft with supersonic wing leading edges and laminar flow technology over the majority of lifting surfaces, the viscous drag due to fuselage is expected to be approximately 20% of the total drag for conventional aircraft planforms and slightly larger, $O(21\%–22\%)$, for low-sweep planforms with supersonic leading edges.¹¹ Thus, keeping the fuselage boundary layer laminar over most of the fuselage nose region would yield a significant reduction in the overall aerodynamic drag. It may be noted that, due to the lower payload fraction for supersonic aircraft (in comparison with subsonic transports), small increases in aerodynamic efficiency can translate into a larger increase in the overall payload.

Unlike wing and empennage boundary layers over the supersonic aircraft, which may be exposed to an increased level of flow disturbances associated with acoustic radiation from turbulent fuselage boundary layers, shock impingement, effects of aerodynamic interference with pylons and nacelles, etc., the boundary layer along the fuselage nose only encounters the external disturbance field from the nominally quiescent region upstream after the disturbance field has been processed by the nose shock. The lower amplitude disturbance environment should make it somewhat easier to maintain a longer region of laminar flow over the fuselage nose. This behavior is different from subsonic fuselage configurations, for which the onset of transition is likely to be influenced by upstream acoustic radiation from the propulsion system.

Practical implementation of natural laminar flow over the fuselage nose requires two separate elements in regard to aerodynamic design and analysis capability: (i) designing a nose shape that tailors the area distribution (i.e., inviscid pressure gradient over the nose surface) to push the transition-onset front as aft as possible while simultaneously helping to minimize the overall drag and boom signature, and (ii) a reliable methodology for transition prediction to minimize the uncertainty in drag reduction.

The simplest canonical shape resembling the nose of a supersonic aircraft corresponds to a circular cone. Extensive wind-tunnel¹² and in-flight¹³ experiments were carried out in the 1960's and early 1970's to examine boundary layer transition over a circular cone of 5-degree half angle from high subsonic to low supersonic Mach numbers ($0.5 \leq M \leq 2$). Particular emphasis was placed on the effect of external disturbance environment on the transition Reynolds number. These measurements did include both zero and small angles of attack, but a majority of the flight data was acquired for a nominally zero angle of attack. The data under axisymmetric conditions has less relevance to transition over the nose of a supersonic aircraft because a typical cruise configuration involves a finite, positive angle of attack. Supersonic transition measurements for cones at finite angle of attack in ballistic range and low disturbance wind tunnel facilities have been reported by Potter¹⁴ and King,¹⁵ respectively. Within the relatively coarse azimuthal resolution of the measurements in [12-15], the earliest onset of transition was observed to occur along the leeward symmetry plane (with the exception of the quiet tunnel measurements in [15] at very small AoA: $\alpha/\theta_c = 0.12$) and the farthest downstream onset along the windward plane, with a generally monotonic variation in transition location as a function of φ in between the two symmetry planes. Malik and Balakumar¹⁶ compared the results of linear stability analysis with the experimentally observed features of transition for $\alpha/\theta_c = 0.4$.¹⁵

The nose shape required for minimum wave drag on a supersonic aircraft is rather different from that of a straight cone. According to slender body theory (i.e., solution of the linearized potential equation), for example, the Sears-Haack (SH) body produces the least wave drag for a given length and maximum diameter. The SH body involves a significantly favorable surface pressure gradient along the streamwise direction, unlike the nominally zero axial pressure gradient for the straight circular cone. The combined effects of nonzero angle of attack and axial pressure gradient on boundary layer transition at supersonic cruise speeds were investigated under an ongoing program of

research between JAXA and NASA. One part of this collaborative program included transition measurements and the accompanying computational analyses for four different nose shapes (namely, Sears-Haack body, semi-Sears-Haack body, 5-degree straight cone and flared cone) at 0- and 2-degree angles of attack.¹⁷ Those measurements were performed by JAXA in two separate, Mach 2 facilities. The other, complementary component involves quiet tunnel measurements and coordinated computations for a 7-degree straight cone. The quiet tunnel measurements will be performed in NASA's Mach 3.5 Supersonic Low Disturbance Tunnel (SLDT).^{18,19} The same SLDT facility had been used during the earlier measurements of transition over a 5-degree straight cone at zero and non-zero angles of attack.¹⁵

The Mach 2 measurements by JAXA¹⁷ revealed the dramatic effect of axial pressure gradient on transition along the leeward plane of symmetry at 2-degree angles of attack. For the SH body with a favorable pressure gradient, no transition was detected along the leeward plane up to at least $R_x \approx 3.6 \times 10^6$, whereas transition occurred within the first half of an equally long flared cone model with an adverse axial pressure gradient. Depending on the facility and/or the unit Reynolds number, the transition Reynolds number along the leeward plane varied from $R_x = 1.14 \times 10^6$ ($R_{unit} = 7.3 \times 10^6 \text{ m}^{-1}$) to $R_x = 1.32 \times 10^6$ ($R_{unit} = 12.2 \times 10^6 \text{ m}^{-1}$). The earlier onset of leeward transition on the flared cone model was in qualitative agreement with the corresponding computations, which had predicted strongly inflectional velocity profiles and substantially higher amplification of linear instability waves along the leeward plane of the flared cone model. However, the N-factor values correlating with the mid-point of transition zone along the leeward plane were unusually large ($N = 10$ and above) in comparison with the lower N-factors ($N \approx 6$) correlating with the measured transition location at zero angle of attack in one of those facilities. There were some additional discrepancies between linear stability predictions and the shape of the experimentally inferred transition fronts near the leeward plane. This paper examines the leeward plane transition in greater detail, as well as investigating the effect of body shape on transition characteristics away from the symmetry planes. In addition, to help provide a better foundation for extrapolating the ground facility data to the low disturbance environment in flight, computations are undertaken for selected conditions from the previously conducted Mach 3.5 quiet tunnel experiments with a 5-degree circular cone.¹⁵

The remaining part of this paper is structured as follows. An overview of the nose shapes selected for this investigation, along with a summary of the experimental measurements is given in Section 2. Mean flow computations for various configurations of interest are presented in Section 3. Results from increasingly higher fidelity computational analysis of transition in the vicinity of the leeward ray are presented in Section 4. Transition over the side region, i.e., in between the windward and leeward planes of symmetry is addressed in Section 5. Summary and concluding remarks are provided in Section 6. The highest fidelity analyses in the form of direct numerical simulations are still ongoing, so this paper constitutes a progress report on the findings thus far.

2 Overview of Flow Configurations

Four different axisymmetric bodies were targeted in the Mach 2 experiments, namely the Sears-Haack (SH) body, a semi-Sears-Haack (SSH) body, a straight cone (SC), and a flared cone (FC). The radius distribution for the SSH body represents a weighted mean of the SH and SC body shapes. The shapes of all four bodies are plotted in Fig. 1, wherein x denotes the axial coordinate relative to the cone apex and R represents the local body radius at a given station. The details of the associated geometry definitions are given by Tokugawa et al.,¹⁷ who also describe the details of experimental measurements in two separate Mach 2 facilities. Table 1 provides a summary of the relevant test cases as well as introducing a composite notation that combines the information about the experimental model, angle-of-attack, and tunnel stagnation pressure. Both adiabatic wall and isothermal wall ($T_w = 300 \text{ K}$, i.e., $T_w/T_{ad} \approx 1.08$) conditions were relevant to these experiments, albeit the difference between the corresponding values of normalized surface temperature (T_w/T_{ad}) was only 8 percent. Mean flow computations were performed for both wall boundary conditions, but the stability analysis for each of those solutions has not been completed as yet. Unless explicitly mentioned otherwise, the results presented in the paper pertain to the nominal conditions listed in Table I.

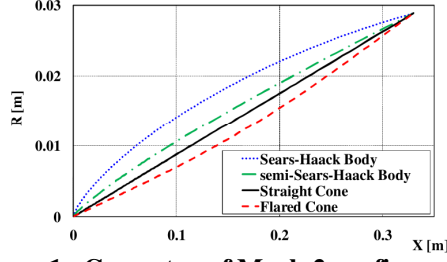


Figure 1. Geometry of Mach 2 configurations.

Table 1: Summary of Mach 2 flow conditions and case notation

Geometric Configuration		Flow Condition	
Shape	Angle of Attack (degrees)	$M=2$	
		$P_0=70\text{kPa}$ $T_\infty=186\text{K}$ $T_w/T_{ad}=1.0$	$P_0=99\text{kPa}$ $T_\infty=165\text{K}$ $T_w/T_{ad}\approx 1.08$
		$R_{unit}/m \approx 7.3 \times 10^6$	$R_{unit}/m = 12.2 \times 10^6$
		Case Notation	
Sears-Haack body (SH) ($L=330\text{mm}$)	2.0	SH-2deg-70	SH-2deg-99
Semi-Sears-Haack body (SSH) ($L=330\text{mm}$)		SSH-2deg-70	SSH-2deg-99
Straight cone (SC) with 5-degree half angle ($L=700\text{mm}$ for SC1, $L=300\text{mm}$ for SC2)	0.0	/	
	2.0	SC2-2deg-70	SC1-2deg-99
Flared Cone (FC) ($L=330\text{mm}$)	2.0	FC-2deg-70	FC-2deg-99

Table 2: Summary of Mach 3.5 flow conditions and case notation for computational solutions

Geometric Configuration		Flow Condition	
Shape	Angle of Attack (degrees)	$M=3.5$	
		$T_0=311\text{K}$ $T_\infty=90.18\text{K}$ $T_w/T_{ad}=1.0$	$T_0=300\text{K}$ $T_\infty=86.96\text{K}$ $T_w/T_{ad}\approx 1.0$
		$R_{unit}/m \approx 7.87 \times 10^6$	$R_{unit}/m = 19.75 \times 10^6$
		Case Notation	
Straight cone (SC) with 5-degree half angle ($L=1.2\text{m}$)	0.0	SC-5-M3.5-0deg	
	0.6	SC-5-M3.5-0.6deg	
	2.0	SC-5-M3.5-2deg	
	4.0	SC-5-M3.5-4deg	
Straight cone (SC) with 7-degree half angle ($L=0.38\text{m}$)	0.0		SC-7-M3.5-0deg
	4.2		SC-7-M3.5-4.2deg

As noted in Table 2, additional computations were performed for a straight cone with 5-degree half angle at flow conditions relevant to the Mach 3.5 experiments in SLDT ($T_0 = 311.1\text{ K}$, $T_w/T_{ad}=1.0$)¹⁵ and a 7-degree half angle cone at conditions relevant to future experiments.^{16,17} The transition Reynolds numbers measured over the 5-degree cone were nearly insensitive to the value of unit

Reynolds number. Accordingly, the unit Reynolds number in the present computations was arbitrarily set to $7.87 \times 10^6 \text{ m}^{-1}$, which is close to the value of $8.2 \times 10^6 \text{ m}^{-1}$ from the computational study in [16]. Computations were performed for each of the four angles of attack used during the experiments, namely $\alpha = 0, 0.6, 2.0,$ and 4.0 degrees. Analogous to the case notation for Mach 2 configurations, the Mach 3.5 cases involving the 5-degree cone are denoted as SC-5-M3.5-0deg, SC-5-M3.5-0.6deg, and so on, where we have suppressed the stagnation pressure from the case notation (since it was constant in all cases and was chosen to yield the targeted Reynolds number) but introduced an additional field to denote the cone half angle to distinguish these cases from the 7-degree cone (Table 2).

3 Mean Flow Solutions

Predictions of instability amplification require an accurate definition of the laminar boundary layer over the various configurations of interest. The laminar basic state for each combination of configuration geometry and flow condition was obtained using numerical solutions to the compressible Navier-Stokes equations. Two different structured-grid flow solvers were used for this purpose, namely, the UPACS²⁰ code developed at JAXA and the VULCAN²¹ solver developed at NASA. Extensive comparisons were made between the UPACS and VULCAN solutions to ensure that the computed mean flow solutions were independent of the code.¹⁷

The laminar boundary layer flow over an axisymmetric body at a nonzero AoA is determined by the axial and azimuthal gradients in the surface pressure, along with the flow Reynolds number and Mach number parameters. The pressure gradient in the axial direction varies with the body shape. As described in [17], the gradient is favorable along the SH and SSH body shapes, but almost zero for the SC and adverse for the FC. Regardless of the body shape, at the small AoA values of interest, there is a positive azimuthal pressure gradient at any fixed axial station. This azimuthal gradient drives a flow from the windward to the leeward side and, hence, causes the boundary layer flow to become fully three-dimensional. Unless the axial flow near the leeward plane accelerates rapidly enough to carry the entire azimuthal flow approaching from both sides of the symmetry plane, the incoming crossflow tends to accumulate near the leeward plane. The accumulation leads to an upwelling near the plane of symmetry (manifested in the form of local increase in the boundary layer thickness),²² and eventually a roll-up of the flow that has been pushed away from the surface. Thus, dramatic variations in the local mean flow structure are possible depending on the body shape as depicted in Figs. 2(a)-(c) for the SH, SC, and FC bodies. Hardly any effects of upwelling in the form of boundary layer thickening near the leeward plane are seen for the SH-2deg-99 case (Fig. 2(a)), whereas a progressive bulge in the boundary layer thickness is noted for successively downstream locations along the straight cone (Fig. 2(b)). For the flared cone, the cumulative effects of upwelling result in a mushroom-shaped structure at sufficiently far downstream locations (rightmost image in Fig. 2(c)). However, the leeward flow is likely to have become turbulent ahead of this station in both conventional and low disturbance facilities. Therefore, the well developed mushroom structure may not be observed in practice.

The boundary layer profiles in the vicinity of the leeward plane are rather sensitive to the grid resolution and, to the best of our knowledge, the grid convergence of leeward profiles in the context of stability analysis has not been demonstrated in the literature. To establish the grid convergence of the basic state profiles, the VULCAN computations used a wide range of grid sizes as illustrated in Figs. 3(a)-(c). The figures indicate the change from non-inflectional velocity profiles for the SH configuration (analogous to the profiles for the axisymmetric case) to mildly inflectional profiles for the SC to strongly inflectional velocity profiles for the FC. Numerically, this change translates into progressively higher resolution requirements to establish grid convergence near the leeward symmetry plane. (Although not shown, even the coarsest of the grids shown in Fig. 3 can adequately resolve the boundary layer profiles away from the leeward plane.) Physically, the observed trend in velocity profile shapes implies stronger amplification of instabilities along the leeward planes of the SC and FC configurations.¹⁷

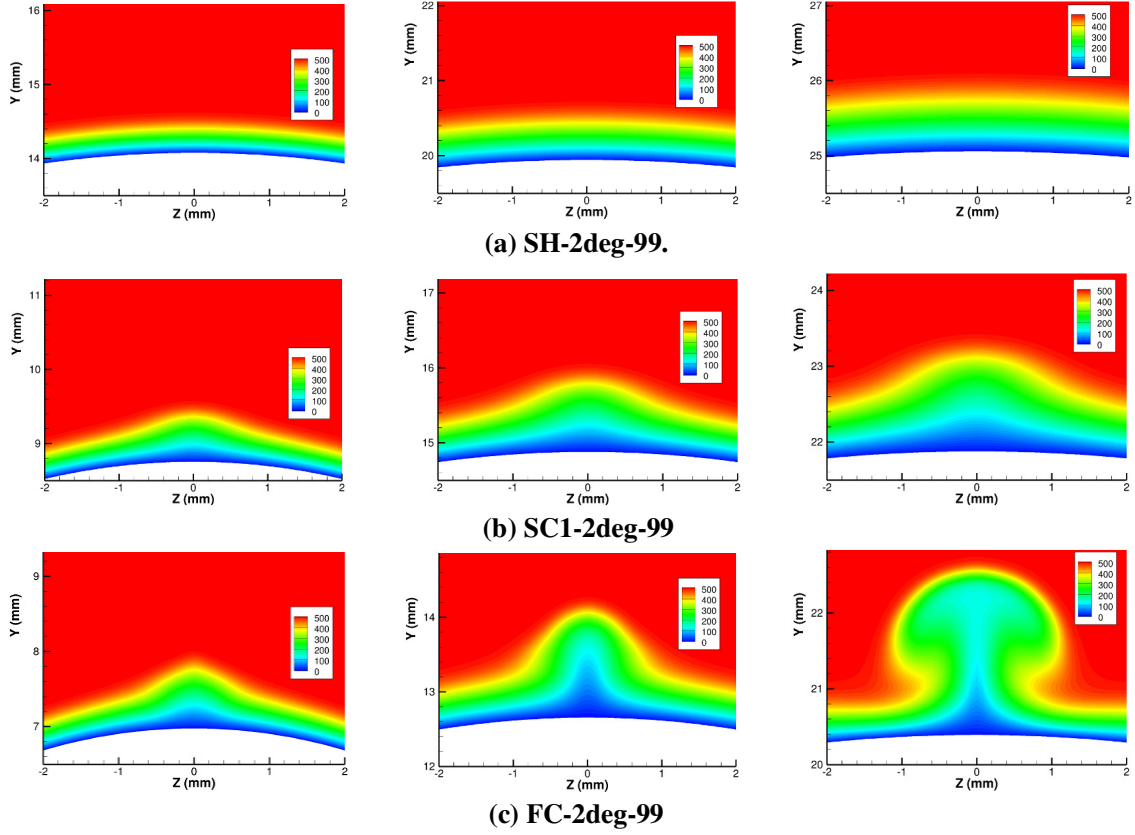
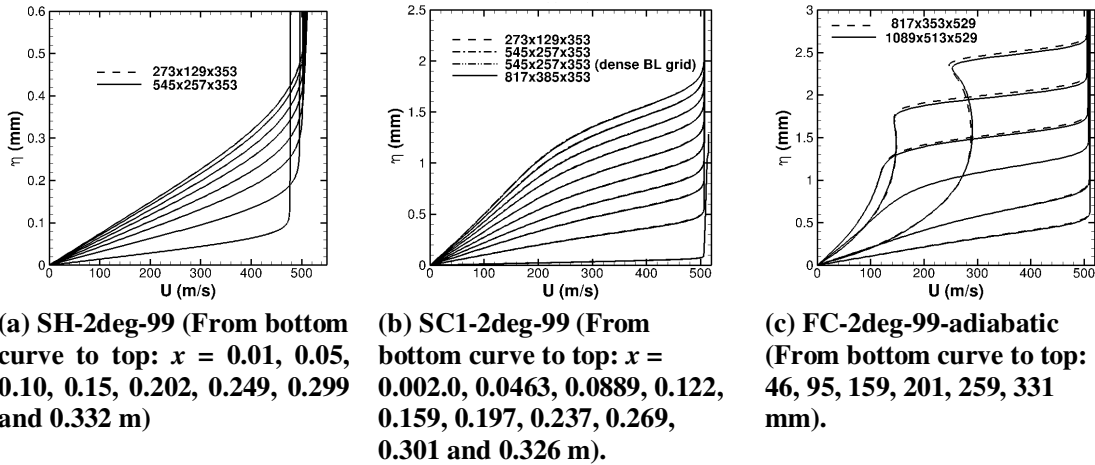


Figure 2. Contours of streamwise velocity (in m/s) in the vicinity of leeward plane for selected Mach 2 configurations (from left to right: $x = 0.1\text{m}$, 0.17m , 0.25m , respectively).



(a) SH-2deg-99 (From bottom curve to top: $x = 0.01$, 0.05 , 0.10 , 0.15 , 0.202 , 0.249 , 0.299 and 0.332 m)

(b) SC1-2deg-99 (From bottom curve to top: $x = 0.002.0$, 0.0463 , 0.0889 , 0.122 , 0.159 , 0.197 , 0.237 , 0.269 , 0.301 and 0.326 m).

(c) FC-2deg-99-adiabatic (From bottom curve to top: 46 , 95 , 159 , 201 , 259 , 331 mm).

Figure 3. Streamwise velocity profiles along the leeward symmetry plane of selected Mach 2 configurations. (The “dense BL grid” in part (b) of the figure had a greater fraction of wall-normal grid inside the viscous region.)

Mean velocity contours and leeward plane profiles for selected Mach 3.5 configurations are shown in Figs. 4 and 5. The differences in velocity contours from Fig. 4 and those seen earlier in Fig. 2(b) for the Mach 2 SC configuration suggest that the details of the leeward flow characteristics may depend on the Mach number to some degree. Case SC-5-M3.5-4deg corresponds to the largest value of the scaled angle of attack ($\alpha/\theta_c = 0.8$) and, hence, the effects of upwelling near the leeward plane appear to be the strongest in this case, being rather prominent even at small axial distances as depicted in Fig.

4(b). Correspondingly, the leeward plane velocity profiles in this case (Fig. 5(b)) acquire a non-monotonic behavior in the outer part of the boundary layer beyond a certain axial distance from the nose, somewhat analogous to the Mach 2 flared cone configuration in Fig. 3(c).

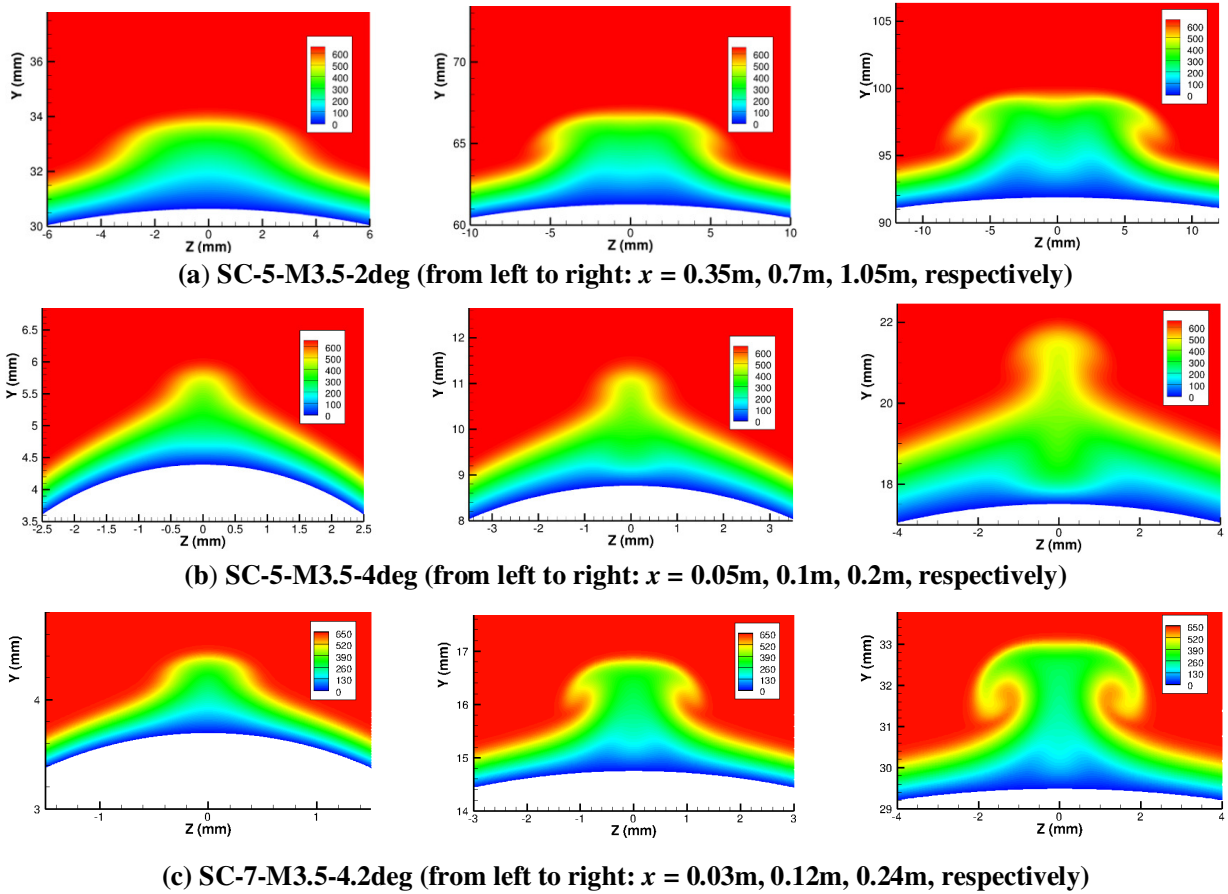


Figure 4. Streamwise velocity contours near leeward symmetry plane of selected Mach 3.5 configurations.

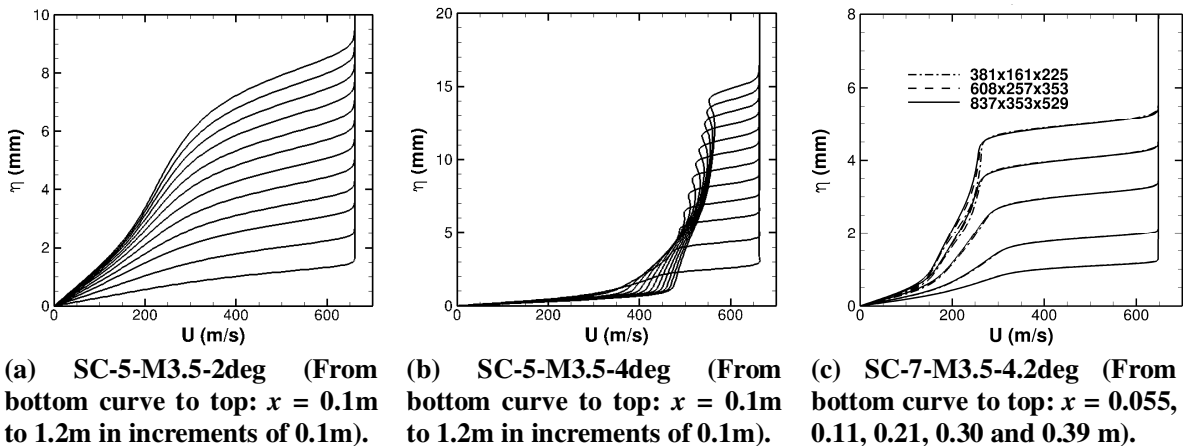


Figure 5. Streamwise velocity profiles along leeward plane of selected Mach 3.5 configurations.

4 Instability Amplification along the Leeward Symmetry Plane

4.1 1-D Linear Stability Analysis

4.1.1 N-factor predictions based on quasi-parallel theory

Quasi-parallel linear stability theory is used for transition analysis using two variants of the N-factor method, namely, the maximum growth envelope and mode tracking methods, respectively. Unless stated otherwise, the effects of both transverse body curvature and streamline curvature are included in these predictions. The basics of the N-factor method are most easily explained for an axisymmetric flow with azimuthally invariant transition front. Essentially, the N-factor method correlates the transition location with the logarithmic amplification ratio (i.e., N-factor) of the most amplified disturbance. This disturbance is determined by taking the envelope of the N-factor curves corresponding to different disturbance frequencies. In one variant of this method that we will refer to as the maximum growth envelope, the N-factor curve for each frequency of interest is determined by integrating the maximum of the local growth rate over all azimuthal wavenumbers n (where n assumes real values). On the other hand, the mode tracking variant of the N-factor method uses the envelope of a two-parameter family of N-factor curves corresponding to different pairs of disturbance frequency f and azimuthal wavenumber n (where n assumes integer values because of the axisymmetric nature of the basic state). The mode tracking method is based on the amplification ratios of nominally independent and physically tractable disturbance entities. While the maximum growth envelope lacks an easily identifiable physical basis, it is computationally less demanding because it maximizes the N-factor over only a single-parameter family of curves, as opposed to the two-parameter family of curves for the mode tracking method, and has been shown to produce reasonable results.²³ Naturally, the N-factor predicted by the maximum growth envelope is somewhat larger than the value based on the mode tracking method.

For 3D flows that are inhomogeneous in both surface directions, such as the present configurations with a nonzero angle of attack, the body surface is parameterized by a suitable set of disturbance evolution trajectories and the N-factor method is applied separately along each of these trajectories. However, because the underlying basic state varies (albeit slowly) along the azimuthal direction, there is no definitive basis for the selection of integration trajectories and the assumption of constant azimuthal wavenumber along the disturbance trajectory also becomes tenuous. Additional ways of applying N-factor analysis to such fully 3D flows have been suggested in the past (see, for instance, Nayfeh²⁴ or the book by Cebeci²⁵); however, there is inadequate knowledge base to determine which of these methods is likely to work better for the present class of flows. The goal in this paper is to assess how predictions based on a subset of the available choices compare with the measured data.

The N-factor values at the measured transition locations over the Mach 2 configurations of interest are listed in the Table 3. The N-factor predictions are based on an adiabatic basic state for both stagnation pressures corresponding to the experiment ($p_0 = 99$ kPa and 70 kPa), even though the model surface temperature for the measurements at $p_0 = 99$ kPa was somewhat higher than the adiabatic surface temperature ($T_w/T_{ad} \approx 1.08$). The effect of surface temperature on the predicted N-factors is estimated in [17]. For more details of the measurements and the methodology used to infer the transition locations, the reader is referred to Tokugawa et al.¹⁷ The left half of Table 3 corresponds to transition along the leeward plane, whereas the right half corresponds to the minimum (or the apex) of the transition front over the side of the cone (i.e., within the region of nonzero crossflow). The discussion of the latter set of results is postponed until Section 5. For the purpose of comparison, results for an axisymmetric straight cone configuration are also included in Table 3. Measured transition locations for the Mach 3.5 configurations (obtained using a digital scan of manually selected points from Figs. 9(a)-(c) from King¹⁵) are summarized in Table 4. As described in Section 5, no local minimum in the transition front was generally discernible in the crossflow region of the Mach 3.5 configurations, at least within the 30-degree azimuthal resolution of the measurements. Thus, the left and right portions of Table 4 correspond to transition along the leeward and windward planes, respectively. The approximate variation in the measured transition Reynolds number at each condition of interest (as determined through the scanning process) and the corresponding variation in the N-factor at the unit Reynolds number used in the computations is indicated in parentheses. In

reality, this variation reflects the effect of unit Reynolds number (within experimental uncertainty) on the transition Reynolds number. However, in the present context, it amounts to an additional source of uncertainty in correlating the N-factor with the measured transition Reynolds numbers.

Table 3: Summary of transition locations and corresponding N factors for Mach 2 Configurations¹⁷

(Measured transition location corresponds to the mid-point of transition-onset and end-of-transition locations; estimated length of transition zone is less than 20% of the distance from nose to transition onset location. Cases where experimental limitations prevented sufficiently accurate inferences regarding transition are left blank)

Configuration	Transition front along leeward plane ($\varphi = 0\text{deg}$)				Apex of transition front within side region			
	x [m]	R_x [million]	N- LSTAB	N- LASTRAC	x [m]	R_x [million]	φ [deg]	N- LSTAB
SC1-0deg-99 (Transition location extrapolated)	0.33	4.29	6.2	5.6	NA			
SH-2deg-99					0.24	3.02	50	9.6
SSH-2deg-99								
SC-2deg-99	0.14	1.79	18.4	16.9	0.12	1.51	35	5.5
FC-2deg-99	0.11	1.32	13.5	10.9	0.15 (at $\varphi = 30\text{deg}$)	1.80	30	6.2
SH-2deg-70	Transition not detected							
SSH-2deg-70					0.21	1.48	30	5.2
SC-2deg-70	0.23	1.65	26.4	NA	0.19	1.41	30	5.1
FC-2deg-70	0.16	1.14	13.6	NA	0.19 (at $\varphi = 30\text{deg}$)	1.40	30	5.1

Table 4: Measured transition onset Reynolds numbers and corresponding N factors for Mach 3.5 Configurations

(The dimensional transition locations (x [m]) are based on the measured transition Reynolds number and the unit Reynolds number used in computations)

Configuration	Transition front along leeward symmetry plane ($\varphi = 0\text{deg}$)			Transition front along windward symmetry plane ($\varphi = 180\text{deg}$)		
	x [m]	R_x [million]	N-LASTRAC	x [m]	R_x [million]	N-LASTRAC
SC-5-M3.5-0deg (quiet)	1.00	7.9	8.0	1.00	7.9	8.0
SC-5-M3.5-0.6deg (quiet)	0.88	6.9 (6.5-7.0)	8.8 (8.5-8.9)	1.03	8.1 (7.7-8.6)	8.6 (8.2-8.9)
SC-5-M3.5-2deg (quiet)	0.32	2.5 (2.5-2.6)	14.3 (14-15)	1.05	8.3 (7.8-8.5)	8.7 (8.4-8.8)
SC-5-M3.5-4deg (quiet)	0.33	2.6 (2.3-2.7)	26.8 (24-28)	1.08	8.5 (7.9-8.7)	9.4 (8.9-9.6)
SC-5-M3.5-0deg (noisy)	0.44	3.45	4.5	0.44	3.45	4.5
SC-5-M3.5-0.6deg (noisy)	0.36	2.9 (2.9-3.1)	4.8 (4.8-5.0)	0.39	3.1 (3.1-3.5)	4.4 (4.3-4.7)
SC-5-M3.5-2deg (noisy)	0.22	1.7 (1.6-1.8)	9.9 (9.5-10.5)	0.57	4.5 (3.7-5.2)	5.6 (4.8-6.1)
SC-5-M3.5-4deg (noisy)	0.20	1.6 (1.6-1.8)	17.9 (17-20)	0.76	6.0 (5.3-6.6)	7.2 (6.5-7.8)

Two separate codes were used for the N-factor predictions, with a partial overlap between the cases analyzed using the two codes as described in [17] in the context of the Mach 2 configurations. All results based on the maximum growth envelope method are obtained using the LSTAB²⁶ code of JAXA, whereas those based on the mode tracking method are obtained with NASA's LASTRAC^{27,28} software. In both calculations, selected streamlines at the edge of the boundary layer are used as the integration trajectories for computing the N-factor curves. Because of the large number of configurations involved, a somewhat coarse grid in the (f, n) space was used for the currently reported N-factor calculations based on the mode tracking method. Thus, the predicted values are believed to be accurate to no more than the first significant digit. However, none of the significant conclusions should be affected by the higher uncertainty in N-factors relative to the predictions based on the maximum growth envelope method.

The following observations can be made on the basis of the results presented in Tables 3 and 4:

1. For a 5-degree half-angle cone at zero AoA, the transition Reynolds number measured by JAXA in Mach 2 facilities is approximately 25 percent higher than that measured in SLDT at Mach 3.5 under noisy conditions (i.e., with no boundary layer suction to keep the nozzle wall boundary layer laminar). The corresponding N-factor at Mach 2 ($N=5.6$) is marginally higher than the Mach-3.5-noisy case ($N=4.5$), although this small difference may not be significant in view of the differences in transition measurement techniques as well as the uncertainty in both experimental measurement and N-factor computation based on the mode tracking method.
2. As discussed by Tokugawa et al.¹⁷, the N-factors for leeward plane transition at Mach 2 (SC and FC configurations) are considerably higher than those in the axisymmetric case discussed above ($N>10$ vs. $N\approx 5$), and they exceed even the N-factor for axisymmetric transition under quiet conditions at Mach 3.5.^{15,29} The N-factors for leeward plane transition are similarly high for the Mach 3.5 configurations with a nonzero AoA, except in the $\alpha = 0.6$ degree case which involves a weak crossflow and, hence, benign mean velocity contours analogous to those in Fig. 2(a) for the Sears-Haack body. Indeed, the transition N-factors in some cases (SC-2deg-99, SC-2deg-70, and SC-5-M3.5-4deg) are unrealistically large for any disturbance environment. This suggests that the growth of instabilities along the leeward plane may be overestimated by the classical stability theory when the AoA is sufficiently large to produce strong effects of crossflow upwelling near the leeward symmetry plane, or that the mean boundary layer profile is less inflectional (i.e., more stable) in the experimental flow than the numerically predicted one.
3. Regardless of the tunnel disturbance environment, the transition Reynolds number along the leeward plane drops rapidly after the AoA is increased from zero, but appears to saturate for $\alpha > 2$ degrees (i.e., $\alpha/\theta_c > 0.8$). The transition Reynolds number along the windward plane increases monotonically with α at least up to $\alpha/\theta_c = 0.8$, albeit at a slower rate than the initial decrease in transition Reynolds number along the leeward plane. This behavior is consistent with the ballistic range data by Potter¹⁴ at similar Mach numbers, as well as with the rather limited flight measurements described in [13]. The mean boundary layer profiles near the windward plane are similar to those in the axisymmetric case (except for the presence of a weak crossflow component) and, hence, no fundamental change in transition physics is expected to be introduced by the modest AoA. Thus, it is somewhat interesting that transition N-factor along the windward plane also appears to increase weakly with AoA over $0 \leq \alpha/\theta_c \leq 0.8$ under both quiet and noisy conditions. The overall change under quiet conditions could, perhaps, be within the combined uncertainty of measurement and computation. However, the corresponding N-factor increase in the noisy case is more significant ($\Delta N \approx 1.7$) and may be due the shift in dominant instability frequencies along with corresponding changes in free-stream disturbance amplitudes associated with the noisy environment. A more detailed discussion of this topic is deferred to a separate study.

The remaining parts of this section focus on refining the instability growth predictions beyond the quasi-parallel stability theory, so as to obtain clues regarding which of the various physical effects neglected within the classical 1D theory might account for the unusually large transition N-factors (and, presumably overpredicted instability growth rates) along the leeward plane. To this end,

parabolized stability equations (PSE) are used first to assess the effects of streamwise variations of mean flow within the leeward plane. Next, in subsection 4.2, the line marching PSE is extended to surface marching PSE to include some of the effects of azimuthal mean flow variations near the leeward plane. Subsection 4.3 outlines the application of an advanced stability model for mean flows that are strongly inhomogeneous in two spatial directions (namely, radial and azimuthal directions in the present case). The final subsection (4.4) considers the effects of nonlinear interactions within the leeward plane, albeit from the limited perspective of nonlinear PSE.

4.1.2 Effect of mean-flow non-parallelism on disturbance growth

The linear form of the parabolized stability equations (PSE) was used for selected pairs of disturbance frequency and azimuthal wavenumber to assess whether or not the effects of mean-flow variations along the streamline trajectory can account for a significant portion of the discrepancy between the N-factor correlations for the axisymmetric case and the leeward plane transition at 2-degree AoA. (Note that the effects of azimuthal mean flow variations are not included in these line marching PSE calculations.) Although not shown, the non-parallel effects are found to be insignificant in the axisymmetric case. A similar finding is observed for instability amplification along the leeward plane of both SC1-2deg-99 and FC-2deg-99 configurations as seen from the rightmost images in Figs. 6(a) and 6(b), respectively.

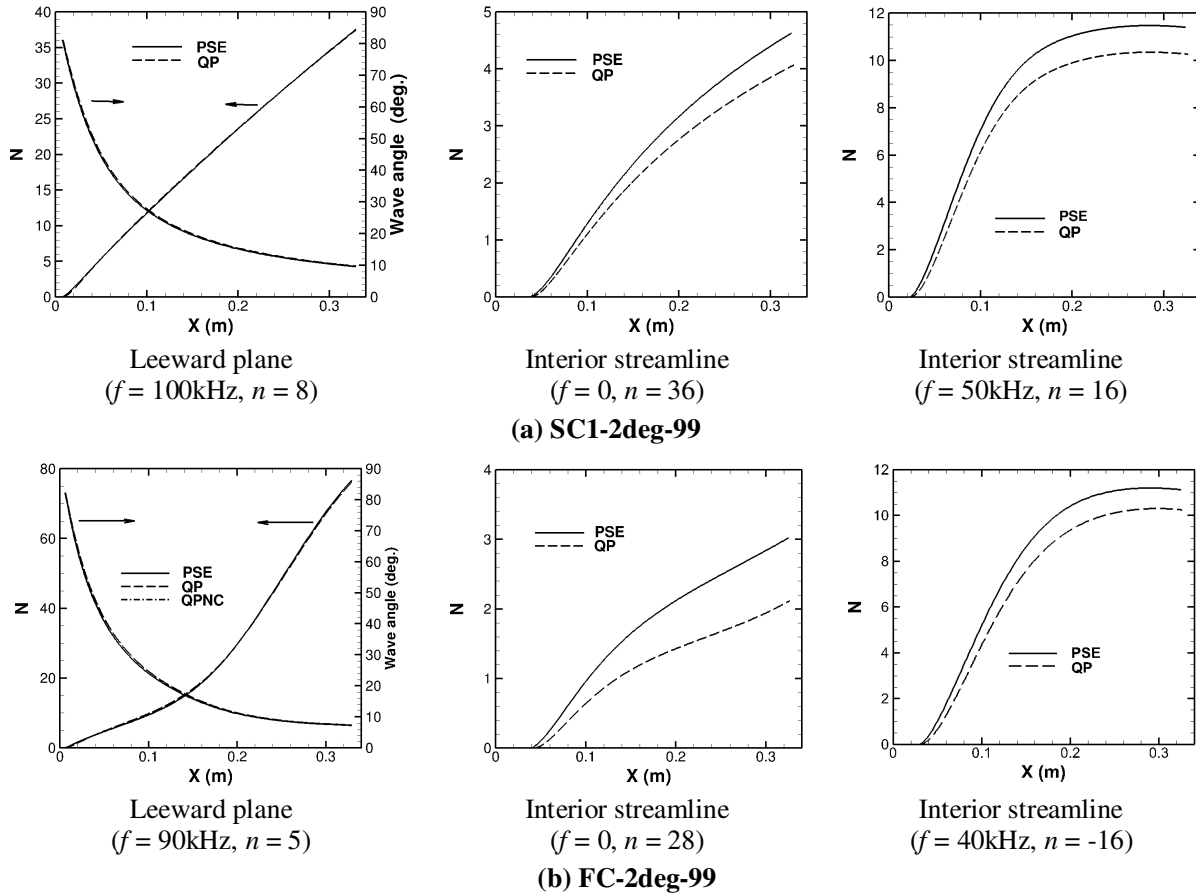


Figure 6. Effect of mean flow non-parallelism on N-factor evolution along leeward ray and a selected interior streamline. (Both stationary crossflow and non-stationary disturbances are considered in latter case.) Disturbance parameters selected for the purpose of illustration correspond to an instability mode with relatively high amplification. Results for the interior streamline are discussed in Section 5.

The results pertaining to the amplification of both stationary and non-stationary disturbances along a selected trajectory on the side of the cone (which is not too far from the streamline passing

through the apex of the transition front in the side region) are also included in the middle and right of Figs. 6(a)-(b), respectively. A discussion of those results is postponed until Section 5.

4.2 Application of Surface Marching PSE

Because of the enhanced significance of azimuthal mean flow gradients in the vicinity of the leeward plane for the SC and FC configurations, it is useful to examine their effect on the instability modes in this region. One way to account for the effect of azimuthal variations in the basic state corresponds to surface marching PSE.²⁸ Predictions based on surface marching PSE analysis are shown in Fig. 7, which displays the contours of linear amplification ratio for a disturbance of fixed frequency ($f = 80$ kHz) and a nominal azimuthal wavenumber of $n = 10$. This disturbance is initiated with a uniform amplitude distribution at $x = 0.0116$ m for all azimuthal locations. The uniform initial amplitude is used as a reference to normalize the computed disturbance amplitudes at the downstream locations, in order to express their evolution in terms of an N-factor distribution. Note that the azimuthal angle is zero at the leeward plane and equals 180 degrees at the windward plane. The amplitude is plotted on a logarithmic scale, relative to the initial amplitude at the left boundary of the computational domain.

As shown, the disturbance amplification is confined in a narrow band near the leeward plane (within about 4-deg azimuthal angle). The large N-factor values computed in this manner (e.g., $N \approx 14$ at the measured transition location of $x = 0.14$ m) are consistent with the quasi-parallel results¹⁷ that predict a rapid growth of first mode instabilities in a narrow, sliver-like azimuthal region in the immediate vicinity of the leeward symmetry plane. Disturbances away from the leeward plane grow rather weakly, with an N factor of about 2. At large enough azimuthal angles, the disturbance growth picks up modestly as the crossflow magnitude increases and the instability mechanism associated with traveling crossflow instability begins to influence the growth rates. The contours away from the leeward plane exhibit some wiggles due to imperfect initial conditions for the PSE surface marching. It should be noted that results obtained from surface-marching for a single azimuthal mode do not represent the overall disturbance growth at the prescribed frequency. A broadband solution obtained via judicious combination of solutions obtained for several azimuthal wave numbers may better represent the disturbance evolution in a 3D boundary layer; however, a computation of this type was deemed beyond the scope of the present effort.

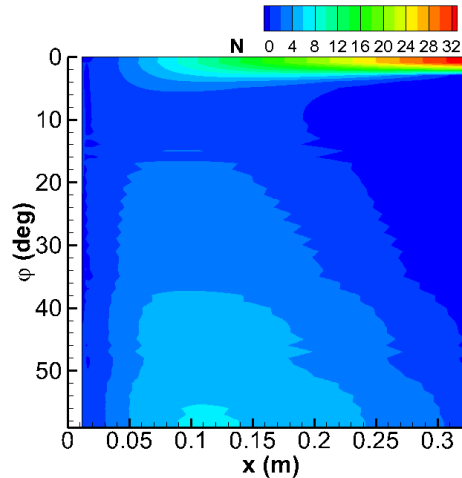


Figure 7. N-factor distribution for disturbance mode with $f = 80$ kHz, $n = 10$ as predicted via surface marching PSE analysis.

4.3 2-D (Planar) Stability Analysis

Since the spanwise and wall normal length scales of boundary layer flow near the leeward plane become increasingly comparable farther downstream along both the straight cone (SC1-2deg-99 at Mach 2 and all Mach 3.5 cases with $\alpha > 2$ degrees) and the flared cone (FC-2deg-99) configurations, the laminar basic state acquires a strongly inhomogeneous character in both wall normal and

azimuthal directions (or, equivalently, in the y and z Cartesian coordinates). While the surface marching PSE technique allows one to account for the effects of both axial and azimuthal gradients of the basic state, the assumption of a disturbance field consisting of a nominally single azimuthal wavenumber becomes questionable due to the coupling between the azimuthal spectrum of the instability wave field and the broader wavenumber content of the localized bulge feature near the leeward plane. An alternate way of accounting for the strong basic state inhomogeneity in both radial and azimuthal directions (or, equivalently, the Cartesian y and z coordinates near the leeward plane) without making any unnecessarily restrictive assumptions about the azimuthal structure of the disturbance field is to examine the instability of the collective “bulge” feature (Figs. 2 and 4) in the vicinity of the leeward plane by solving an eigenvalue problem based on two-dimensional (i.e., planar) partial differential equations (PDEs).^{30,31} The key assumption underlying the planar instability analysis is that the quasi-cylindrical (or quasi-conical) nature of the bulge feature enables the unstable perturbations at any given x to be characterized in terms of a single streamwise wavenumber and a single amplification rate. Because of the abrupt change in boundary layer thickness from the bulge region to the region away from the leeward plane, we choose to focus attention on unstable eigenmodes that are concentrated near the leeward plane and hence do not involve any coupling with the outer azimuthal region. This PDE based analysis is rather different from the conventional linear stability analysis, which is based on the assumption of basic state homogeneity in φ , which leads to a locally periodic eigenmode structure (i.e., with a non-compact support) in the azimuthal direction.

Spatial stability of the computed leeward flow was examined at three selected streamwise locations along the FC-2deg-99 configuration. These locations bracket the measured transition location ($x \approx 0.11\text{m}$) in the experiment by JAXA¹⁷ and would also be relevant to transition in a low disturbance environment. Due to the base flow symmetry at the leeward plane, both even (i.e., symmetric) and odd (i.e., antisymmetric) disturbance modes must be analyzed separately as indicated in Figs. 8(a)-8(b), respectively. To allow comparison with the 1D, quasi-parallel stability predictions underlying the relatively large N-factor values in Table 3, the 1D growth rate predictions for a selected value of n are also included in Figs. 8(a)-(b). The azimuthal wavenumber ($n = 5$) selected for the 1D predictions falls within the wavenumber range corresponding to the highest N factors at the selected locations. Furthermore, the changes in 1D growth rates due to modest variations from $n = 5$ are relatively small.

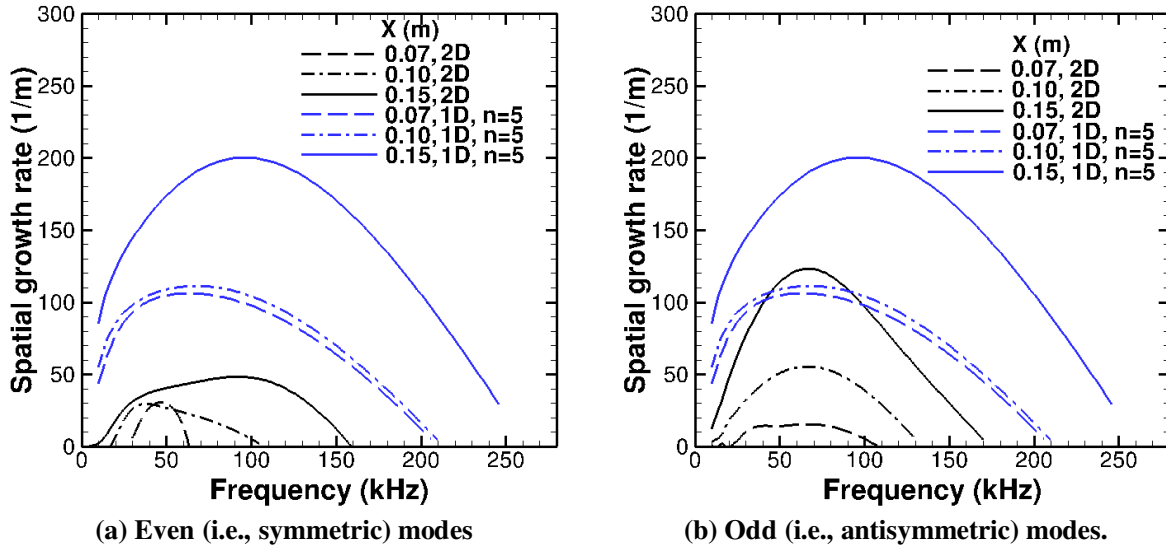


Figure 8. Variation of local growth rate with frequency at selected streamwise stations for case FC-2deg-99.

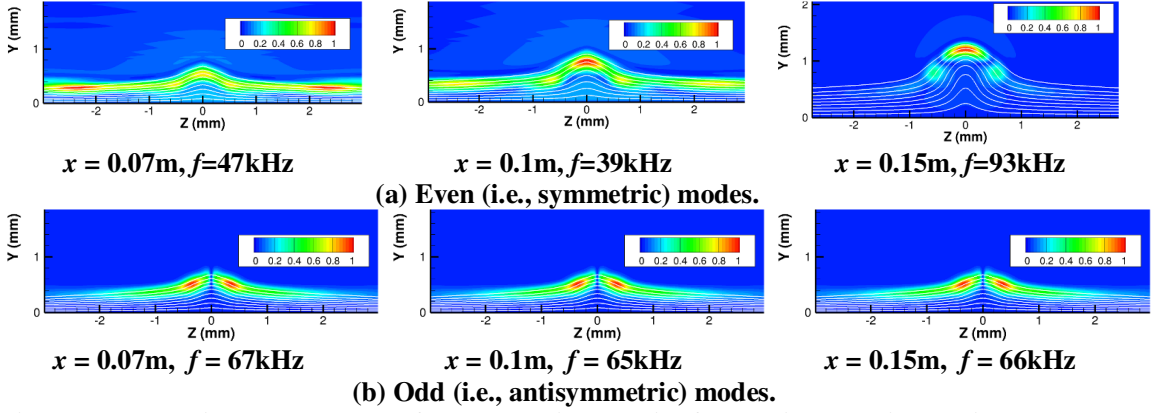


Figure 9. Normalized mode shapes for streamwise velocity fluctuation associated with planar modes in the vicinity of peak growth frequency at selected axial stations for configuration FC-2deg-99.

In general, only a single unstable mode of each type was found at every selected station, with the exception of the farthest downstream station ($x = 0.15\text{m}$) where two separate unstable modes of the even type were encountered. The highest growth rate of the odd unstable mode is more than twice the peak growth rate of the even modes and the peak growth rate increases with x as the effects of basic state upwelling become more prominent. Figures 8(a)-(b) also indicate that the frequency range corresponding to each mode type broadens at farther downstream stations as the bulge feature becomes stronger. Yet, the frequency range of unstable disturbances based on the planar eigenvalue analysis is narrower than the range predicted by the 1D theory. More important, however, the peak growth rate of the odd modes based on planar eigenvalue computation is substantially smaller than the peak growth rates predicted by the 1D theory (by a factor of nearly 2 at $x = 0.1\text{m}$). Thus, if the PDE based eigenvalue analysis provides better estimates of disturbance growth near the leeward symmetry plane, then the peak N-factor at the measured transition location would be significantly smaller than the 1D correlation and, hence, more in line with the N-factor values for axisymmetric configurations.

The normalized mode shapes corresponding to the magnitude of streamwise velocity fluctuation at selected disturbance frequencies (close to the peak growth rate frequency at each axial station) are shown in Figs. 9(a)-(b). Inspection of the mode shapes at $x = 0.1\text{m}$ and $x = 0.15\text{m}$ indicates that the peak fluctuations associated with the even and odd modes are concentrated within separate regions of high basic state shear in the vicinity of the $z = 0$ plane. At $x = 0.15\text{m}$, i.e., when the localized bulge in the mean velocity contours has become sufficiently prominent, the mode shape for the even mode disturbance is highly localized near the symmetry plane. This indicates a decoupling of the disturbance motions near and away from the leeward plane. In contrast, significant levels of fluctuation are observed in the outer portions of the even mode shape at $x = 0.07\text{m}$ and 0.1m . The expanded mode shape signature indicates that the numerical boundary conditions used to isolate the leeward region for the purpose of planar instability analysis (along with, perhaps, the basic premise of treating the neighborhood of the leeward plane as a single entity) become somewhat questionable when the bulge is not sufficiently prominent. A more sophisticated model based on tracking the evolution of a known initial disturbance using the linearized Navier-Stokes equations may become necessary in those cases, at least for the even mode computations. For the odd modes, on the other hand, the fluctuation magnitude decays smoothly away from the peak in the vicinity of the leeward plane.

Such intricacies of the instability characteristics in the vicinity of the leeward symmetry plane and the reduction in the associated growth rates relative to 1D stability predictions indicate the need to exercise caution while using the classical theory alone to draw inferences regarding the growth of unstable perturbations in the vicinity of the leeward symmetry plane. Future direct numerical simulations are planned to evaluate the predictions based on the planar eigenvalue analysis presented in this subsection. However, well-resolved off-body flow-field measurements analogous to those of Kegerise et al.³² behind a discrete roughness element in a lower Mach number flow would go a long way in providing a definitive confirmation of the computational observations in this section.

4.4 Oblique Breakdown

The discussion of leeward plane instabilities thus far has focused on their linear growth characteristics. However, the onset of transition must be preceded by nonlinear interactions contributing to the establishment of random, broad-band, 3D vortical motions and fuller mean velocity profiles. A laminar breakdown scenario common to 2D/axisymmetric supersonic flows involves the oblique mode breakdown^{33,34} initiated by the nonlinear interactions between a pair of oblique, first-mode disturbances with equal but opposite wave angles. A similar scenario might occur for the transition process along the leeward plane at nonzero AoA. The latter case is distinguished from the axisymmetric case by (i) a localized region of high wall-normal shear in the basic state profiles away from the wall (recall Figs. 2(b)-(c)), (ii) the azimuthal gradients in the basic state near the leeward plane, and (iii) the relatively smaller values of n corresponding to peak N-factors at the transition location. The smaller values of n imply smaller wave angles and an even greater disparity between the boundary layer thickness and the azimuthal wavelength of the oblique disturbance in comparison with the typical values for axisymmetric flows, i.e., in the absence of boundary layer upwelling. It is conceivable that the weaker three-dimensionality of the primary disturbance impedes the creation of the smaller spanwise scales required for the onset of turbulence, and that the resulting delay in transition accounts for the higher N-factors noted by Tokugawa et al.¹⁷

To allow the modeling of oblique mode breakdown along the leeward plane in the simplest possible context, i.e., within the purview of conventional nonlinear PSE for mean flows that are homogeneous in the azimuthal direction, an effectively axisymmetric basic state was generated by replicating the leeward plane profiles at nonzero AoA over the 60-degree azimuthal wavelength of a pair of oblique disturbances with $n = \pm 6$ and $f = 100$ kHz in the SC1-2deg-99 case. To minimize the effects of the neglected azimuthal variations in the basic flow, the disturbance amplitudes were selected to be somewhat large so that transition onset could occur when the cumulative effects of upwelling near the leeward symmetry plane were still relatively small compared to those just upstream of the measured transition location. Two different initial amplitudes of the primary disturbance (measured in terms of the peak R.M.S. fluctuation in streamwise velocity at the initial station) were considered, namely, $A_{init} = 10^{-4}$ and 10^{-5} , respectively. The axial evolution of the modal amplitudes corresponding to different Fourier harmonics in the (f, n) space are shown in Fig. 10(a) for $A_{init} = 10^{-5}$. No symmetry breaking perturbations were imposed at the inflow plane; hence, only the modal amplitudes corresponding to Fourier harmonics within the first quadrant ($f > 0, n > 0$) are shown in the figure. The evolution of the broadband R.M.S. fluctuation amplitude for both initial amplitudes is shown in Fig. 10(b) and the corresponding variation in total wall shear is plotted in Fig. 10(c).

The evolution of modal amplitudes in Fig. 10(a) is typical of the oblique breakdown process in 2D/axisymmetric mean flows. The initial evolution is dominated by the oblique fundamental harmonics with normalized indices of $(1, \pm 1)$. Their nonlinear interaction generates the stationary $(0, \pm 2)$ component with streamwise vorticity, which in turn generates the $(1, \pm 3)$ modes. These nonlinearly excited disturbances amplify rapidly and eventually overtake the amplitudes of the primary, fundamental harmonics. The onset of transition (marked by the rapid rise in wall shear in Fig. 10(c)) occurs close to the point of crossover and also in the vicinity of the location marked by a faster increase in the broadband fluctuation amplitude (Fig. 10(b)). The initially benign crossplane contours of R.M.S. velocity fluctuation (Fig. 10(d)) acquire a greater structure (Fig. 10(e)) as the spanwise varying peak-valley structure of the mean flow distortion becomes sufficiently strong near the predicted location of wall shear increase. Because of the relatively large azimuthal wavelength of the primary disturbance, it appears that the onset of breakdown may well be localized in the azimuthal direction, requiring a spreading of the turbulent kinetic energy before a fully developed turbulent flow can set in.

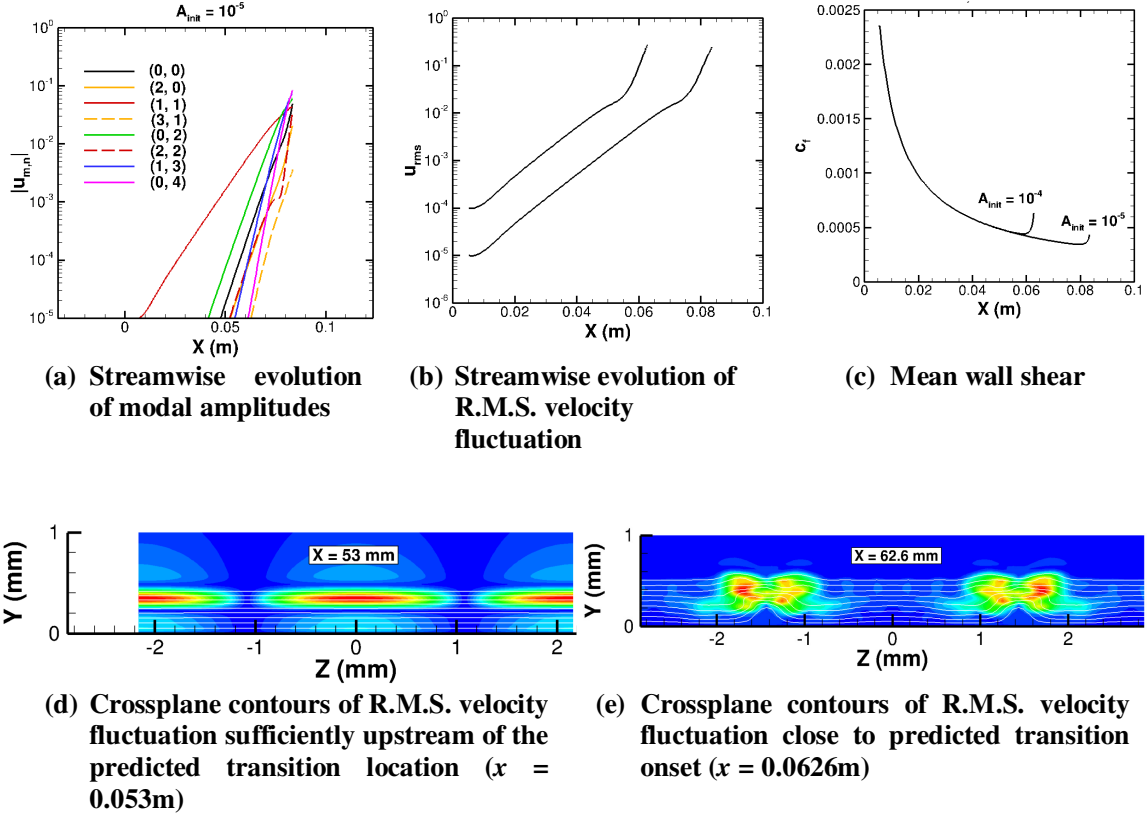


Figure 10. Oblique mode breakdown in leeward plane boundary layer of SC1-2deg-99 configuration ($f = 100\text{kHz}$, $n = \pm 6$, $A_{init} = 10^{-5}$ unless explicitly indicated otherwise).

Similar to the PDE based stability analysis, the above nonlinear PSE analysis incorporates the interactions among multiple azimuthal modes within the Fourier expansion of the disturbance field. However, the mean flow variation in the azimuthal plane and the resulting coupling between the azimuthal modes is neglected in these computations. To simulate the strongly nonlinear bulge near the leeward plane, such variation must be accounted for in the azimuthal Fourier expansions.

The overall similarity between the oblique breakdown process in Fig. 10 for the leeward plane boundary layer and that of 2D and axisymmetric boundary layer flows suggests that the explanation for the higher N-factor values correlating with the measured onset of transition in the Mach 2 facilities is not likely to be due to any differences in the nonlinear phase of transition. More sophisticated computations that account for the azimuthal variations in basic state near the leeward plane will be undertaken in the future to confirm this speculation.

5 Instability Amplification over the Region of Nonzero Crossflow

N-factor contours for selected Mach 2 configurations are included in Figs. 11(a) through 11(f), along with approximate transition fronts extracted from the IR measurements described by Tokugawa et al.¹⁷ The light brown circles in these figures indicate the transition front based on the top view of the model, whereas the dark brown circles indicate the transition front inferred from the side view of the model under the same flow conditions. Two separate scalar measures of the overall transition front were extracted from the results in Fig. 11, namely transition location on the leeward ray (indicated by an open diamond in Fig. 11) and the earliest location along the side lobe (indicated by a circle), and are listed in Table 3. The transition locations for the FC-2deg-99 and FC-2deg-70 configurations are monotonically increasing functions of the azimuthal angle φ from the leeward ray and, hence, the minimum of the side lobe could not be identified. Therefore, the location at $\varphi = 30$ degrees was listed in Table 3. The growth rate integration trajectories used for N-factor calculation are illustrated for the SC1-2deg-99 case in Fig. 11(c). The effects of mean flow variations along the

integration trajectory were illustrated in Figs. 6(a) and 6(b) for both stationary (middle plot in each figure) and nonstationary (right plot) development along a representative interior streamline within the crossflow region of the SC1-2deg-99 and FC-2deg-99 configurations, respectively. These effects were seen to be modestly destabilizing, in general, with a larger relative N-factor increment in the case of stationary crossflow modes.

The following observations can be made in relation to Fig. 11:

1. The measurements by Tokugawa et al.¹⁷ provide a clear indication of a local minimum in the transition front within the crossflow region for all body shapes, except for the flared cone. In contrast, with the exception of the SC-5-M3.5-0.6deg case corresponding to a rather low value of AoA, a number of previous ground facility-based transition front measurements for supersonic flows over axisymmetric bodies at nonzero incidence^{14,15} had indicated that the transition location moves monotonically upstream as the azimuthal location varies from the windward to the leeward plane. Thus, the JAXA data^{17,39,40} as shown in Fig. 11 provide the first definitive evidence that transition fronts with an interior minimum can be frequently observed within the above class of supersonic flows. (A similar feature in transition front had also been detected during temperature sensitive paint measurements on a delta wing configuration;⁴¹ however, the body shape involved was fully three-dimensional and, hence, the flow topology was likely to have been different from the axisymmetric configurations targeted herein.)
2. Even though the N-factor curves in Fig. 11 do not distinguish between the different types of instability modes in the boundary layer, these flow configurations support multiple instability mechanisms, namely first mode, stationary crossflow, and traveling crossflow instabilities. The relative significance of each mechanism varies with azimuthal location along the body surface, the body geometry, flow conditions, and the disturbance environment. For example, crossflow is identically zero along the symmetry planes, but potentially dominant around $\varphi = 60$ deg at modest AoA.¹⁶ Mixed-mode transition (i.e., with two or more modes of instability playing an important role) is also a possibility, especially near regions of switchover in the dominant instability mechanism. Furthermore, details of surface roughness in the neighborhood of the neutral stability locations close to the nose (specifically, at azimuthal locations corresponding to an approximate zone of dependence of the measured transition location) can also have an impact on the transition location, along with the unsteady disturbances in the free stream. This complexity of the mixed-mode transition process may be the underlying reason for why there is no clear trend in transition N-factors across the various configurations. From the practical standpoint of physics-based predictions, however, it is somewhat encouraging that, except in a small region adjacent to the leeward plane, the measured transition fronts are often bracketed between the contours corresponding to $N=5$ and $N=9$ for the nonstationary modes, with a narrower spread within a few cases.
3. For the straight cone configuration, the minimum transition Reynolds number at 2-degree AoA is lower than that at 0-degree AoA by a factor of between 2 and 3. Also, at the fixed AoA of $\alpha = 2$ degrees, the transition Reynolds numbers for the SH configuration are substantially larger than those for the SC and FC configurations. However, the lack of transition data for the SSH body (as well as potential differences in surface roughness of the different models) prevents a definitive conclusion regarding the effect of body shape on the minimum transition location within the side region. The qualitative change in the overall shape of the transition front from the SH configuration to the FC configuration has, however, been attributed to the differences in the leeward plane stability characteristics.¹⁷

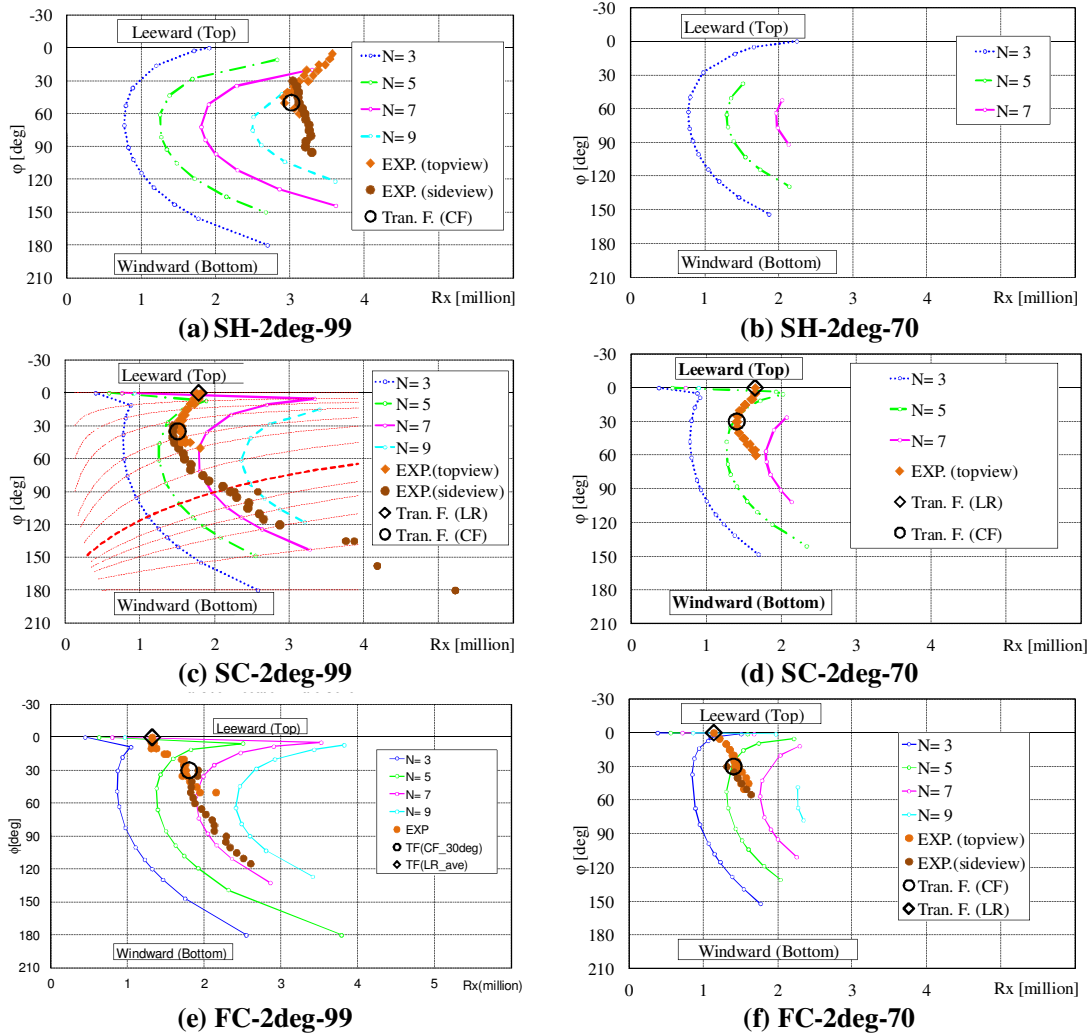


Figure 11. N-factor contours based on maximum growth envelope method for selected Mach 2 configurations.

The measured transition fronts for Mach 3.5 configurations, along with the N-factor contours for non-stationary and stationary disturbances are shown in Figs. 12 and 13, respectively. Unlike the results in Fig. 11, which were based on the maximum growth envelope, the results at Mach 3.5 are based on the mode tracking method. The following observations/speculations can be made on the basis of the results from Figs. 12 and 13:

1. Regardless of the type of dominant primary instability in different regions of the cone surface, the free-stream disturbance environment plays an important role in determining the transition location. The difference between transition N-factors for quiet and noisy modes of wind tunnel operation appears to be highest near the windward symmetry plane.
2. For $\alpha = 0.6$ deg, the peak N-factors for stationary crossflow instability are too low ($N < 1$) for transition to occur via the stationary modes (Fig. 13(a)). At $\alpha = 4$ deg, $N > 5$ for stationary modes over a significant portion of the measured transition fronts and even approach $N = 12$ for the measured transition front under quiet conditions (Fig. 13(c)), making it likely that the stationary vortices play a significant role during the transition process over at least a portion of the cone surface. In regard to N-factors for stationary disturbances, the $\alpha = 2$ deg case (Fig. 13(b)) falls in between the other two cases, so whether or not the stationary crossflow modes play an important role during transition will depend (even more) on the relative initial amplitudes of the stationary and nonstationary disturbances which, in turn, are determined by the surface finish characteristics and the free stream disturbance environment.

3. The increased significance of stationary crossflow instability at $\alpha = 2$ deg and $\alpha = 4$ deg may be reflected in the reduced difference between the transition Reynolds numbers corresponding to noisy and quiet conditions for azimuthal locations corresponding to sufficiently strong crossflow magnitudes.
4. At all three AoA, the transition N-factor decreases at first as one moves from the windward plane towards the middle of the cone (where crossflow is maximum and there is also a nearby minimum in the constant-N contours) and then decreases again as one moves further towards the leeward plane. It is not clear whether the latter decrease at lower azimuthal angles may be attributed to a potential interaction between stationary and nonstationary disturbances.

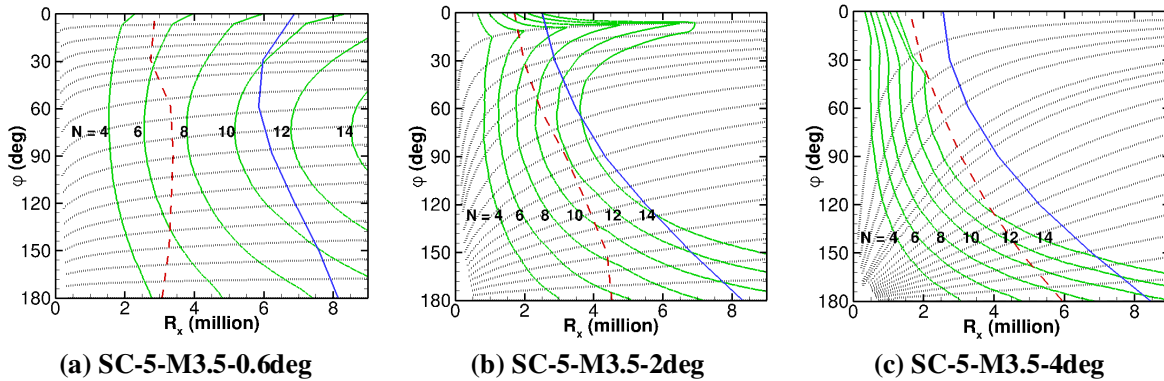


Figure 12. N-factor contours for nonstationary disturbances based on maximum growth envelope method for Mach 3.5 configurations. (Green curves: contours of constant N-factor; black dotted lines: selected integration trajectories for N-factor calculation; blue curve: measured transition front under low disturbance conditions; red dashed curve: measured transition front under noisy conditions; all measurements taken at 30 deg azimuthal spacing)

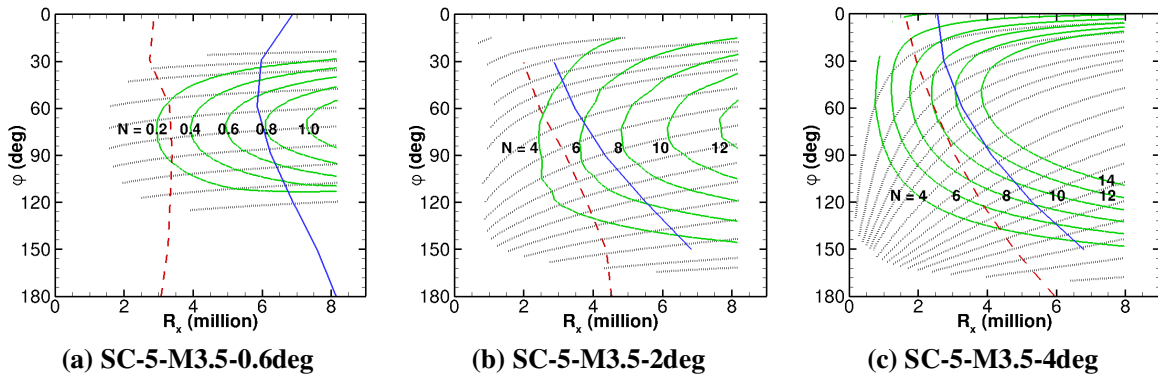


Figure 13. Same as Figure 13, except that N-factor contours for stationary disturbances are shown.

6 Summary and Concluding Remarks

Boundary layer transition along the leeward symmetry plane of axisymmetric bodies at a non-zero angle of incidence in supersonic freestream was investigated via experiments and numerical computations as part of joint research between JAXA and NASA. Transition over four axisymmetric bodies (namely, Sears-Haack body, semi-Sears-Haack body, straight cone and flared cone) with different streamwise pressure gradients was studied. The experimental results reported in a companion paper¹⁷ established the strong effects of axial pressure gradient on the transition behavior near the leeward symmetry plane. Furthermore, the accompanying computations outlined in [17] had shown that the earlier transition along the leeward plane under non-favorable axial pressure gradients

was caused by the increasingly thicker and more strongly inflectional (and correspondingly more unstable) boundary layer profiles along the leeward symmetry plane. However, when conventional, 1D stability theory was used for correlating with transition along the leeward plane, the resulting N-factor values were found to be unusually high in comparison with N-factors for the same models at zero AoA and the typical range of N-factors for experiments on similar configurations in facilities without any form of boundary layer control to maintain laminar flow along the nozzle walls. In this paper, highly accurate basic state computations are used to reveal the dependence of leeward plane profiles on the fully three-dimensional dynamics associated with the interaction between streamwise pressure gradient and the accumulation of secondary flow along the leeward plane. Data from a synergistic series of previously reported NASA experiments at Mach 3.5¹⁵ was examined using linear stability predictions to confirm some of the findings from the JAXA experiments¹⁷ and to obtain additional insights into those findings.

Several candidate hypotheses to explain the large N-factor values based on quasi-parallel stability theory for leeward plane transition were examined in this paper, including streamwise variation of the mean flow, weak nonparallel effects associated with azimuthal gradients of the base flow in the vicinity of the leeward plane, unstable perturbations of the strongly inhomogeneous, quasi-cylindrical region of a locally thickened boundary layer, and differences in oblique mode breakdown due to somewhat unique characteristics of the leeward plane instabilities. Only the second to the last hypothesis, involving an advanced, partial-differential-equation based eigenvalue analysis associated with the strongly inhomogeneous basic state variations within the crossplane, indicated the possibility of significantly reduced instability growth rates (and, hence, lower values of transition N-factors) along the leeward plane. Further work is necessary to confirm this hypothesis more definitively.

Except in a small region adjacent to the leeward plane, the measured portion of the transition fronts in the Mach 2 experiments was usually bracketed between the contours corresponding to $N=5$ and $N=9$ for the nonstationary modes (barring a correction associated with exact surface temperature at experimental conditions), with a narrower spread within a few cases. Furthermore, the body shape of the axisymmetric configuration appeared to have a less dramatic effect on transition within the side (i.e., crossflow) region than on the transition behavior in the vicinity of the leeward plane, except perhaps for the delayed onset of transition on the Sears Haack body. To help achieve an extended region of laminar flow within the crossflow region, it will be useful to consider the combined effects of streamwise and azimuthal pressure gradients (i.e., 3D shaping) during the optimization of the nose shape for the fuselage of a supersonic aircraft.

Overall, this paper has provided an assessment of linear stability based transition correlations for canonical slender body configurations relevant to natural laminar flow over the nose region of a supersonic aircraft. Selected features of the existing data pertaining to leeward plane transition have been explained, but there exist other discrepancies (or significant scatter in transition-factors) in regard to the transition behavior within the crossflow region for angles of attack corresponding to $0.12 < \alpha/\theta_c < 0.8$. Additional work targeting some of those issues is currently ongoing.

Acknowledgments

The JAXA authors would like to thank Dr. K. Yoshida for his valuable advice. They also acknowledge the support for experiments from Mr. H. Sugiura, Dr. S. Koike, and Dr. K. Nakakita of JAXA, along with Mr. T. Murayama, Mr. A. Nose and Mr. K. Fujisaki from Gakushuin University. The work at NASA was performed as part of the Supersonic Cruise Efficiency -- Airframe discipline of the Supersonics Project of NASA's Fundamental Aeronautics Program (FAP). Technical discussions with Dr. M. Malik, Dr. R. Rubinstein, Mr. S. Wilkinson, Mr. L. Owens, and Dr. P. Balakumar at NASA Langley Research Center are also acknowledged.

References

- [1] Joslin, R. D., "Aircraft laminar flow control," *Ann. Rev. Fluid Mech.*, Vol. 30, 1998, pp. 1-29.
- [2] Carpenter, A. L., Saric, W. S., and Reed, H. L., "Laminar Flow Control on a Swept Wing with Distributed Roughness," AIAA Paper 2008-7335, 2008.

- [3] Powell, A. G., "The Right Wing of the L.E.F.T. Airplane," NASA CP 2487, 1987, pp. 141–61.
- [4] Maddalon, M. D. and Braslow A. L., "Simulated-airline-service flight tests of laminar-flow control with perforated-surface suction system," NASA TP 2966, 1990.
- [5] Collier F. S. Jr., "An Overview of Recent Subsonic Laminar Flow Control Flight Experiments," AIAA Paper 93-2987, 1993.
- [6] Anders, S. G. and Fischer, M. C., "F-16XL-2 Supersonic Laminar Flow Control Flight Test Experiment," NASA TP-1999-209683, 1999.
- [7] Norris, G., "Hybrid Help," *Aviation Week & Space Technology*, Vol. 172, Issue 30, 8/9/2010, p. 36.
- [8] <http://hondajet.honda.com/designinnovations/index.aspx>, Oct. 21, 2011.
- [9] Tokugawa, N., Kwak, D. Y., Yoshoda, K., and Ueda, Y., "Transition Measurement of Natural Laminar Flow Wing on Supersonic Experimental Airplane NEXST-1," *J. Aircraft*, Vol. 45, No. 5, 2008, pp. 1495-1504.
- [10] Vijgen, P. M. H. W., Dodbele, S. S., Holmes, B. J., and Van Dam, C. P., "Effects of Compressibility on Design of Subsonic Fuselages for Natural Laminar Flow," *J. Aircraft*, Vol. 24, No. 5, May 1987, pp. 298-304.
- [11] Kroo, I., "Unconventional Configurations for Efficient Supersonic Flight," *VKI lecture series on Innovative Configurations and Advanced Concepts for Future Civil Aircraft*, June 6-10, 2005.
- [12] Dougherty, N. S. and Fisher, D. F., "Boundary Layer Transition on a 10-degree Cone: Wind Tunnel/Flight Data Correlation," AIAA Paper 80-1054, 1980.
- [13] Dougherty, N. S., Jr., and Fisher, D. F., "Boundary Layer Transition Correlation on a Slender Cone in Wind Tunnels and Flight for Indications of Flow Quality," AEDC TR-81-26, Feb. 1982.
- [14] Potter, J. L., "Boundary-Layer Transition on Cones Near Mach One in an Aeroballistic Range," AEDC TR-74-115, Jan. 1975.
- [15] King, R. A., "Three-Dimensional Boundary-Layer Transition on a Cone at Mach 3.5," *Experiments in Fluids*, Vol. 13, 1992.
- [16] Malik, M. and Balakumar, P., "Instability and Transition in Three Dimensional Supersonic Boundary Layers," AIAA Paper 92-5049, 1992, pp. 305-314.
- [17] Tokugawa, N., et al., "Transition along Leeward Ray of Axisymmetric Bodies at Incidence in Supersonic Flow," AIAA Paper 2012-3259, 2012.
- [18] Owens, L., Kegerise, M., and Wilkinson, S. "Off-Body Boundary-Layer Measurement Techniques Development for Supersonic Low-Disturbance Flows," AIAA Paper 2011-284, 2011.
- [19] Balakumar, P., "Stability of Supersonic Boundary Layers over a Cone at an Angle of Attack," AIAA Paper 2009-3555, 2009.
- [20] Yamazaki, H., Enomoto, S. and Yamamoto, K., "A Common CFD Platform UPCAS," *High Performance Computing*, Lecture Notes in Computer Science, Vol. 1940, 2000, pp. 182-190.
- [21] Litton, D. K., Edwards, J. R. and White, J. A., "Algorithmic Enhancements to the VULCAN Navier-Stokes Solver," AIAA 2003-3979, June, 2003. (Also: <http://vulcan-cfd.larc.nasa.gov> (Aug. 18, 2011))
- [22] Lin T. C. and Rubin, S. G., "Viscous Flow over a Cone at Moderate Incidence. Part 2. Supersonic Boundary Layer," *J. Fluid Mech.*, Vol. 59, 1973, pp. 593-620.
- [23] Malik, M. R., "Instability and Transition in Supersonic Boundary Layers," *Laminar-Turbulent Boundary Layers*, Proceedings of Energy Resources Technology Conference, edited by E. M. Uram and H. E. Weber, American Society of Mechanical Engineers, New York, Feb. 1984, pp. 139-147.
- [24] Nayfeh, A. H., "Stability of Three-Dimensional Boundary Layers," *AIAA J.*, Vol. 18, No. 4, 1980, pp. 406-416.
- [25] Cebeci, T., *Stability and Transition: Theory and Application : Efficient Numerical Methods with Computer Programs*, Horizons Pub., Long Beach, CA, and Springer, Heidelberg, Germany, 2004.

- [26] Ueda, Y., Ishikawa, H., and Yoshida, K., "Three Dimensional Boundary Layer Transition Analysis in Supersonic Flow Using a Navier-Stokes Code," *Proceedings of International Congress of the Aeronautical Science 2004-2.8.2*, [CD-ROM], 2004.
- [27] Chang, C.-L., "Langley Stability and Transition Analysis Code (LASTRAC) Version 1.2 User Manual," NASA/TM-2004-213233, 2004.
- [28] Chang, C.-L., "LASTRAC.3d: Transition Prediction in 3D Boundary Layers," AIAA Paper 2004-2542, 2004.
- [29] Chen F.-J., Malik, M. R., and Beckwith, I. E., "Boundary-layer transition on a cone and flat plate at Mach 3.5," *AIAA Journal*, Vol. 27, No. 6, 1989, pp. 687-693.
- [30] Li, F. and Choudhari, M., "Spatially Developing Secondary Instabilities and Attachment Line Instability in Supersonic Boundary Layers," AIAA Paper 2008-590, 2008. (also: Li, F. and Choudhari, M., "Spatially Developing Secondary Instabilities in Compressible Swept Airfoil Boundary Layers," *Theoretical and Computational Fluid Dynamics*, Vol. 25, 2011, pp. 65-84.)
- [31] Choudhari, M., Chang, C.-L., Jentink, T., Li, F., Berger, K., Candler, G., and Kimmel, R. L., "Transition Analysis for the HIFiRE-5 Vehicle," AIAA Paper 2009-4056, 2009.
- [32] Kegerise, M., King, R., Owens, L. Choudhari, M., Norris, A., Li. F. and Chang, C.-L. "Wake Instability Behind a Discrete Roughness Element in High Speed Boundary Layers," Paper 28, *ATV-200 Specialist Meeting on Hypersonic Transition*, San Diego, CA, April 2012.
- [33] Fasel, H., Thumm, A., and Bestek, H., "Direct Numerical Simulation of Transition in Supersonic Boundary Layer: Oblique Breakdown," *Transitional and Turbulent Compressible Flows*, edited by L. D. Kral and T. A. Zang, No. 151 in FED, ASME, 1993, pp. 77-92.
- [34] Chang, C.-L. and Malik, M. R., "Oblique-Mode Breakdown and Secondary Instability in Supersonic Boundary Layers," *J. Fluid Mech.*, Vol. 273, 1994, p. 323-360.
- [39] Murayama, T., Nose, A., Tokugawa, N., Ishikawa, H., and Fujisaki, K., "Compressive Boundary-Layer Transition near the Top-Line of an Axisymmetric Body at Incidence," *Proceedings of 2007 Annual Meeting, Japan Society of Fluid Mechanics*, [CD-ROM], 2007 (in Japanese).
- [40] Sugiura, H., Tokugawa, N., Nishizawa, A., Ueda, Y., Ishikawa, H., and Yoshida, K., "Boundary-Layer Transition on Axisymmetric Bodies with Angles of Attack in Supersonic Flow," *Proceedings of 2003 Annual Meeting, Japan Society of Fluid Mechanics*, 2003, pp.352-353 (in Japanese).
- [41] Cattafesta, L. N., III, Iyer, V., Masad, J. A, King, R. A., and Dagenhart, J. R., "Three-Dimensional Boundary-Layer Transition on a Swept Wing at Mach 3.5," *AIAA Journal*, Vol. 33, No. 11, 1995, pp. 2032-2037.